Journal of Inorganic Biochemistry 260 (2024) 112681

Contents lists available at ScienceDirect

Journal of Inorganic Biochemistry

journal homepage: www.elsevier.com/locate/jinorgbio

Entrance channels to coproheme in coproporphyrin ferrochelatase probed by exogenous imidazole binding

Andrea Dali [a], Thomas Gabler [b], Federico Sebastiani [a], Paul G. Furtmüller [b], Maurizio Becucci [a,c,*], Stefan Hofbauer [b,**], Giulietta Smulevich [a,d,*]

[a] Dipartimento di Chimica "Ugo Schiff" (DICUS), Università di Firenze, Via della Lastruccia 3-13, I-50019 Sesto Fiorentino (FI), Italy
[b] BOKU University, Department of Chemistry, Institute of Biochemistry, Muthgasse 18, A-1190 Vienna, Austria
[c] The European Laboratory for Non-Linear Spectroscopy (LENS), Via Nello Carrara 1, I-50019 Sesto Fiorentino (FI), Italy
[d] INSTM Research Unit of Firenze, Via della Lastruccia 3, I-50019 Sesto Fiorentino (FI), Italy

ARTICLE INFO

Keywords:
Heme protein
Resonance Raman spectroscopy
Imidazole titrations
Kinetic analysis
X-ray diffraction
Binding sites

ABSTRACT

Iron insertion into porphyrins is an essential step in heme biosynthesis. In the coproporphyrin-dependent pathway, specific to monoderm bacteria, this reaction is catalyzed by the monomeric enzyme coproporphyrin ferrochelatase. In addition to the mechanistic details of the metalation of the porphyrin, the identification of the substrate access channel for ferrous iron to the active site is important to fully understand this enzymatic system. In fact, whether the iron reaches the active site from the distal or the proximal porphyrin side is still under debate. In this study we have thoroughly addressed this question in *Listeria monocytogenes* coproporphyrin ferrochelatase by X-ray crystallography, steady-state and pre-steady-state imidazole ligand binding studies, together with a detailed spectroscopic characterization using resonance Raman and UV–vis absorption spectroscopies in solution. Analysis of the X-ray structures of coproporphyrin ferrochelatase-coproporphyrin III crystals soaked with ferrous iron shows that iron is present on both sides of the porphyrin. The kinetic and spectroscopic study of imidazole binding to coproporphyrin ferrochelatase-iron coproporphyrin III clearly indicates the presence of two possible binding sites in this monomeric enzyme that influence each other, which is confirmed by the observed cooperativity at steady-state and a biphasic behavior in the pre-steady-state experiments. The current results are discussed in the context of the entire heme biosynthetic pathway and pave the way for future studies focusing on protein-protein interactions.

1. Introduction

Heme *b* is a crucial iron-containing prosthetic group of many essential proteins [1] which facilitates several functions. For instance, bacterial pathogens need to synthesize heme *b* to survive, while infecting the host [2]. In 2015 Dailey and co-workers [3] discovered that monoderm bacteria synthesize heme *b* using the coproporphyrin-dependent (CPD) biosynthesis pathway [4]. Differently, diderm bacteria predominately use the protoporphyrin-dependent (PPD) heme pathway [5], similarly to eukaryotes. Although the two pathways share the same initial substrate, coproporphyrinogen III, they produce heme *b* differently. Detailed overview figures of both pathways can be found in the literature [4–8].

In both pathways, ferrochelatases (fCs) are fundamental enzymes, that catalyze ferrous iron insertion into tetrapyrrole rings [5,9,10]. In the CPD heme biosynthesis, coproporphyrin ferrochelatase (CpfC) inserts ferrous iron into coproporphyrin III to yield ferric iron-coproporphyrin III (coproheme). Then, in the final step of the pathway, the coproheme decarboxylase generates heme *b* by a two-step decarboxylation of the propionate groups at positions 2 (p2) and 4 (p4)

Abbreviations: bis-Im complex, imidazole bound to both the proximal and distal coordination positions of the coproheme iron; *Bs*CpfC, CpfC from *Bacillus subtilis*; CPD, coproporphyrin-dependent; CpfC, coproporphyrin ferrochelatase; fC, ferrochelatase; HS, high spin; Im, imidazole; IS, intermediate spin; *Lm*CpfC, CpfC from *Listeria monocytogenes*; LS, low spin; Mb, myoglobin; p2, p4, p6, p7, propionate groups at position 2, 4, 6 or 7; PPD, protoporphyrin-dependent; PpfC, protoporphyrin ferrochelatase; RR, resonance Raman; WT, wild type; 4c, tetracoordinated; 5c, pentacoordinated; 6c, hexacoordinated.

* Corresponding authors at: Dipartimento di Chimica "Ugo Schiff" (DICUS), Università di Firenze, Via della Lastruccia 3-13, I-50019 Sesto Fiorentino (FI), Italy.
** Corresponding author at: BOKU University, Department of Chemistry, Institute of Biochemistry, Muthgasse 18, A-1190 Vienna, Austria.
E-mail addresses: maurizio.becucci@unifi.it (M. Becucci), stefan.hofbauer@boku.ac.at (S. Hofbauer), giulietta.smulevich@unifi.it (G. Smulevich).

https://doi.org/10.1016/j.jinorgbio.2024.112681
Received 17 May 2024; Received in revised form 25 July 2024; Accepted 27 July 2024
Available online 30 July 2024

of the coproheme pyrrole ring, forming vinyl groups, with the concomitant release of CO_2 [11–15]. Differently, in the PPD heme biosynthesis, the protoporphyrin ferrochelatase (PpfC) inserts ferrous iron into protoporphyrin IX to produce heme *b*. Therefore, PpfC and CpfC are active at different stages of their respective pathways and utilize different substrates, i.e. protoporphyrin IX and coproporphyrin III, respectively [5,16]. As coproporphyrin III differs from protoporphyrin IX by the presence of p2 and p4 and the absence of any vinyl groups [5], these enzymes present differences in conserved amino acids of the active site to bind the correct substrate [7,17–20].

Recently we have shown that CpfC from *Listeria monocytogenes* (*Lm*CpfC) is capable of completely forming coproheme, starting from the physiological substrate (i.e., coproporphyrin III) but it is only partially active on other substrates as protoporphyrin IX [7,21]. The impaired capability to produce heme *b* is correlated with the loss of interaction between the protein and both p2 and p4 (absent in protoporphyrin IX), which results in a weaker binding to the active site of the enzyme as compared to the physiological substrate. The impact of the H-bond interactions between the propionate groups of coproporphyrin III or coproheme and the protein on catalysis and stabilization of the porphyrin was investigated using several site-directed variants, selectively lacking these H-bonds [7,18]. These interactions were found to be fundamental for the correct binding of the substrate and product as well as for the stabilization of the active site of the enzyme.

Additionally to the role of the propionate groups, we have also investigated the influence of the key distal and proximal residues in the active site [21,22]. On the proximal site, the X-ray crystallographic structure of the native *Lm*CpfC complexed with coproheme [17] indicates the presence of a tyrosine (Tyr12) residue (Fig. 1) 2.7 Å away from the coproheme iron and positioned almost parallel to the porphyrin ring, with a potential π-stacking interaction with the pyrrole ring A. Tyr12 acts in solution as the proximal ligand of iron resulting in a pentacoordinated high spin (5cHS) complex [21,22]. On the distal site, the structure shows a histidine and glutamate pair (namely, His182 and Glu263 in *Lm*CpfC numbering) (Fig. 1), which are highly conserved in all fCs [6]. Different authors postulated that these residues are essential for the iron insertion process [20,23–26]. However, our recent results suggest that neither His182 nor Glu263 are essential for the metalation of the porphyrin; instead, the glutamate residue was found to be involved in the iron oxidation process of the product [21]. Also the propionate groups seem to have a major role during the iron insertion process. Using X-ray crystallography and resonance Raman (RR) spectroscopy we have observed and described a reorientation and relocation of the propionate groups during metalation with the formation of a stable, saddle-distorted reaction intermediate species (both in the crystal and solution). The distortion then slowly decreases, as the propionate groups establish the interaction typical of the almost planar coproheme complex [27].

However, the metalation process is a complex mechanism and its details, which are still a matter of debate, need further investigation [28,29], particularly in bacterial enzymes. An open question remains about the ferrous iron's entry site, i.e., whether the ferrous iron approaches from the proximal or the distal side. A study on CpfC from *Bacillus subtilis* (*Bs*CpfC) shows an iron atom bound to the distal His and Glu [30]. However, the results were obtained by soaking the *Bs*CpfC apoprotein with ferrous iron and so, with no porphyrin inside the active site of the enzyme. Moreover, mutational, and mechanistic studies on yeast, murine and human PpfCs suggest that other divalent cations, such as Zn^{2+} and Cd^{2+}, can bind on the distal site [19,24,31,32]. On the contrary, recent computational and experimental studies have suggested that, for the human fC, the ferrous iron can approach from the proximal side [26,33], which holds a methionine residue at the respective proximal position. This question was further addressed in *Bs*CpfC [34], but it is still not clear to date whether this conclusion can be applied also to bacterial fCs in general, having a Tyr (Firmicutes) or Phe (Actinobacteria) as potential proximal ligands and a different substrate (coproporphyrin III).

Here we address the question of the entry path of the iron (either from the distal or proximal side of the porphyrin) towards the active site of bacterial CpfCs by a comprehensive multi-technique approach. We report an X-ray diffraction experiment on wild-type (WT) *Lm*CpfC – coproporphyrin III crystals upon soaking with ferrous iron, in which we analyse the anomalous electron densities derived from the metal insertion. Furthermore, we present a combined spectroscopic and kinetic analysis of *Lm*CpfC in its coproheme-bound form while binding exogenous imidazole upon titration. Using this non-native binding agent of the porphyrin we demonstrate that both the proximal and distal site's entry paths are accessible. In particular, we have characterized the imidazole binding not only to the WT *Lm*CpfC-coproheme complex but also to other variants, where the proximal Tyr12 was replaced with a His (Y12H variant), His182 with an Ala, and Glu263 with a Gln (H182A and E263Q variants, respectively), in both their ferric and ferrous forms.

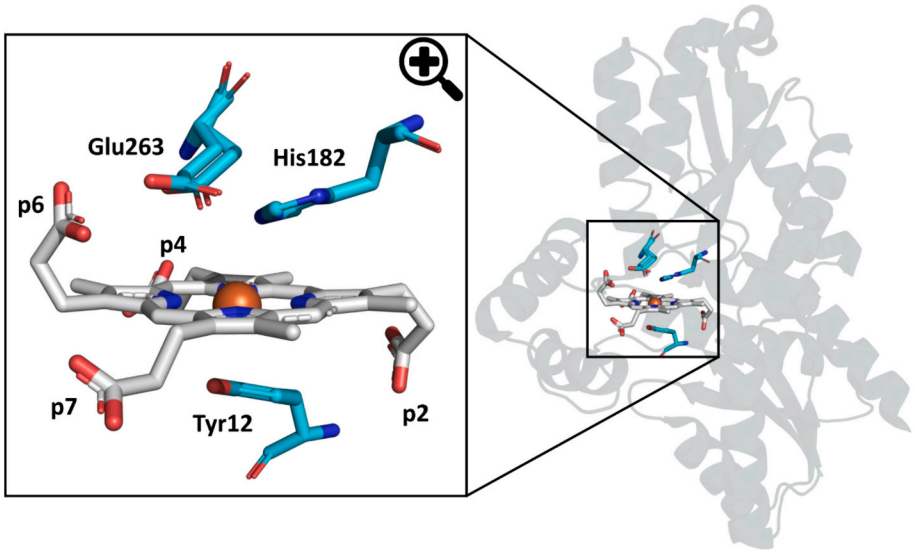

Fig. 1. Active site of WT *Lm*CpfC – coproheme complex. Overall crystallographic structure of wild type (WT) *Lm*CpfC – coproheme (PDB ID: 6SV3) complex (left) and active site (right) highlighting the proximal Tyr12 and the distal residues His182 and Glu263. The propionate groups at positions 2, 4, 6 and 7 (p2, p4, p6 and p7) are also indicated.

These results allow us to highlight the possible role of the proximal Tyr12 and of both the distal His182 and Glu263 in the modulation of the entry channels.

2. Materials and methods

2.1. Generation, expression, and purification of WT and variants of *Lm*CpfC

The generation, expression, and purification of *Lm*CpfC wild-type and variants (namely Y12H, H182A and E263Q) were performed as previously reported [7,17,22].

2.2. Crystallization and soaking

*Lm*CpfC H182A variant in complex with iron coproporphyrin III was crystallized in 13.455% (w/v) PEG 3350, 0.2 M $MgCl_2$ and 0.1 M BIS-TRIS pH 5.5, while WT coproporphyrin III - complex was crystallized in 17.455% (w/v) PEG MME 2000, 0.2 M $CaCl_2$ and 0.1 M BIS-TRIS pH 6.3, as previously described [18]. The H182A iron coproporphyrin III - complex crystals, with a solution equal to the crystallization conditions containing 20% glycerol as cryoprotectant, were flash-vitrified in liquid nitrogen. The WT coproporphyrin III - complex crystals were treated similarly, but the solution contained beside the crystallization components both 20% glycerol as cryoprotectant and 1 mM Fe^{2+}. The crystals were soaked for about three minutes in the solution prior to flash-vitrification in liquid nitrogen. The Fe^{2+} was added shortly before the soaking procedure from a Fe^{2+} stock solution which was anaerobically prepared as previously described [27].

2.3. X-ray data collection, structure determination and refinement

The beamline ID-23-1 was used to collect the dataset for the WT coproporphyrin III with Fe^{2+} crystal at 1.70074 Å using a DECTRIS EIGER 2 16 M CdTe detector and ID-23-2 for the H182A iron coproporphyrin III dataset at 0.87313 Å using a DECTRIS EIGER X 9 M detector both at the European Synchrotron Radiation Facility (Grenoble, France). Both datasets were processed using the EDNA_proc pipeline and data quality was evaluated by Xtriage. The phase problem was solved by molecular replacement with Phaser MR [35] using the pdb structure of *Lm*CpfC WT with coproporphyrin III (PDB ID: 8AT8) and *Lm*CpfC WT with iron coproporphyrin III (PDB ID: 6SV3). For the Fe^{2+} containing WT coproporphyrin III structure refinement, anomalous X-ray scattering data were collected and used to confirm the presence of the metal ion. Any further refinement steps for both datasets were done as previously reported in detail [27]. We used MolProbity [36] to validate the models and PyMOL to generate the images (http://www.pymol.org) with standard settings, and orthoscopic = 1, ray_shadows = 0. In particular, we employed 'set_valence, 1' to depict carboxyl groups as resonance Lewis structures.

2.4. Sample preparation for UV–vis and RR experiments

Ferric coproheme (Frontier Scientific Inc., Logan, UT, USA), solubilized in 0.5 M NaOH, was added to *Lm*CpfC apoprotein, diluted in buffer 0.2 M HEPES, pH 7.4 or 0.3 M BIS TRIS PROPANE pH 8.5 (Table S1). Working at an alkaline pH was useful to increase the stability of the imidazole adducts under the experimental conditions used. An apoprotein:coproheme ratio of 1.5:1 for the WT and E263Q variant or 3:1 for the H182A and Y12H variants was used to avoid the presence of free coproheme in the samples. The addition of imidazole, to the desired final concentration, was made in small aliquots starting from a 1 M imidazole solution in 50 mM HEPES buffer pH 7.4. The ferrous complexes were prepared at pH 7.4 and 8.5 (Table S1), upon reduction of the ferric imidazole adducts with a freshly prepared sodium dithionite solution (20 mg/mL), after degassing with nitrogen.

The sample concentrations, determined as previously reported in [7], were in the range of 40–80 μM for the ferric imidazole adduct and 40–70 or 70–150 μM for the ferrous samples measured using the 404.8 and 441.6 nm excitation wavelengths, respectively.

2.5. UV–vis electronic absorption spectroscopy

The UV–vis absorption measurements were performed in a 1 mm cuvette or a 5 mm NMR tube using a Cary60 spectrophotometer (Agilent, Santa Clara, CA, USA) with a resolution of 1.5 nm and a 300 nm/min scan rate.

The second derivative spectra were calculated using the Savitzky-Golay method on 15 data points with a third-order polynomial (LabCalc, Galactic Industries, Salem, NH). There were no variations in the wavelength or bandwidth when the number of points was changed in the range 9–17. All the spectra were normalized to the maximum intensity of the Soret band and then, the 475–700 nm region was magnified by 5 times, if not otherwise indicated in the figures.

2.6. Resonance Raman (RR) spectroscopy

RR spectra of the samples, inside a slowly rotating 5 mm NMR tube, were obtained by excitation using the 404.8 nm line of a diode laser (MatchBox Series, Integrated Optics, Vilnius, Lithuania) or the 441.6 nm excitation of a He-Cd laser (Kimmon IK4121R-G, Tokyo, Japan). The backscattered light from the sample was focused into a triple spectrometer (Acton Research, Acton, MA-USA) consisting of two SpectraPro 2300i instruments that work in subtractive mode, and a SpectraPro 2500i instrument in the final stage with a grating of 3600 grooves/mm or 1800 grooves/mm and equipped with a liquid nitrogen-cooled CCD detector (Mod. 7346–0001, Roper Scientific Princeton Instruments). A nominal resolution of 1.2 cm^{-1} or 4 cm^{-1} was calculated for the 3600 or 1800 grooves/mm, respectively.

Indene and carbon tetrachloride were used as standards to calibrate the RR spectra wavenumbers to an accuracy of 1 cm^{-1}, for intense isolated bands. The power on the sample was 7 or 2.5 mW for the ferric and ferrous samples, respectively. To enhance the signal-to-noise ratio, the RR measurements were performed several times under the same experimental conditions, and then summed if there were no spectral differences (Table S1). The RR spectra were baseline corrected and normalized in the high wavenumber region to the intensity of the ν_4 band (1358–1377 cm^{-1}) and in the low wavenumber region to the intensity of the ν_8 band (338–350 cm^{-1}). The spectral contribution of free imidazole was subtracted from the spectra.

2.7. Imidazole binding activity, determination of binding and kinetic constant

The capability of WT and variants of *Lm*CpfC – coproheme complex of binding imidazole was monitored by the spectral shift from *Lm*CpfC – coproheme complex to the imidazole-bound form. The complete binding (saturation) was ensured by no further spectral changes in the UV–vis spectra upon the addition of excess imidazole. The imidazole was added in small steps, under continuous stirring, to a 1 mL cuvette. The UV–vis spectra were obtained, three minutes after the imidazole addition, using a Cary60 spectrophotometer (Agilent, Santa Clara, CA, USA) (resolution: 1.5 nm and scan rate: 300 nm/min). The change in absorbance (f), on the maximum of the Soret band, was plotted versus the imidazole concentration (x) and fitted using the Hill equation ($f = y_0 + \frac{ax^n}{c^n + x^n}$), where n is called the Hill coefficient and a is the absorbance at ligand saturation. In the absence of cooperativity between the binding sites $n = 1$, otherwise for positive or negative cooperativity we expect $n > 1$ or $n < 1$, respectively. For the sake of clarity, a positive cooperativity indicates that the binding of the first ligand increases the affinity of the second binding site, whereas negative cooperativity implies that the first

binding of the ligand decreases the affinity of the second binding site. Moreover, the c^n factor of the Hill equation is equal to the dissociation constant K_D.

Time-resolved imidazole binding was monitored using a stopped-flow instrument with a monochromator and a photomultiplier detector (Pistar-180; Applied Photophysics, Leatherhead, UK) equipped with a 75 W Xenon lamp (406 nm) or a Hg-Xe lamp (366 and 404 nm) working at room temperature. The volume of the optical quartz cell was 20 μL with a 10 mm path length. The fastest mixing times were in the range of 1–1.5 ms. Time traces were recorded in triplicates at single wavelengths (366 nm for E263Q, 404 nm for WT and Y12H and 406 nm for H182A) and fitted by two single exponential functions to determine the observed pseudo-first order rate constants (i.e. k_{obs1} and k_{obs2} in s^{-1}). Finally, the association rate constant (i.e. k_{on} in mM^{-1} s^{-1}) was determined from the slope of the plot of the measured k_{obs}-values versus the imidazole concentration.

All these experiments were performed using 5 μM coproheme complex samples prepared as described below (see *Sample preparation for UV–vis and RR experiments*). The used buffers were: 50 mM HEPES buffer pH 7.4 (WT and H182A, E263Q variants of *Lm*CpfC); 0.3 M BIS TRIS PROPANE buffer pH 8.5 (WT and Y12H variants of *Lm*CpfC) to reproduce the condition used for the RR experiment. A slight excess of apo *Lm*CpfC was used with respect to the apoprotein:coproheme ratio suggested below (see *Sample preparation for UV–vis and RR experiments*) to ensure pure spectral species of the protein complex [7,22].

3. Results

We have performed X-ray crystallization soaking experiments, where the WT *Lm*CpfC - coproporphyrin III crystals were soaked with a ferrous iron solution for three minutes, as already reported [27]. The soaked crystals diffracted to 2.1 Å and data collection and refinement statistics are summarized in Table S2. We have exploited the anomalous X-ray scattering of iron to localize possible binding sites. In Fig. 2 the active site structure, including the electron density maps, is depicted showing several electron densities that can be assigned to iron (pink meshes). The most prominent signal is the one found in the center of the porphyrin, as part of the coproheme product. Interestingly, the proposed regulatory site [37] on the distal entry pathway, next to Glu271, is fully occupied with iron. In previously solved crystal structures, the electron density at this position has been filled and interpreted with other divalent ions being present in the storage buffer or crystallization conditions (e.g. Ca^{2+}, Mg^{2+}) [17,19,38].

Further anomalous electron density blobs are observed on the distal side between the conserved His182 and Glu263. This evidence is in agreement with previous studies on iron bound to CpfC from *Bacillus subtilis*, although in the absence of a porphyrin (PDB ID: 2HK6) [20]. It is worth mentioning that also other divalent metal ions are possibly binding to this site of *Bs*CpfC crystals, when appropriate soaking experiments are performed (Co^{2+}, PDB ID: 3M4Z; Zn^{2+}, PDB ID: 1LD3 [19]). Noteworthy, in our samples another anomalous signal from Fe^{2+} ions is further identified on the proximal side of the porphyrin in close proximity to Tyr12, albeit of smaller intensity.

As the results obtained from the X-ray crystallography soaking experiments do not provide a clear answer to the initial question on the iron entry path towards the active site, we have designed an experimental model system to probe the possible substrate access channels to the active site. We have, therefore, performed ligand binding studies using imidazole on the *Lm*CpfC - coproheme complex. The imidazole titration has been followed by UV–vis and resonance Raman spectroscopies, as well as its kinetics under steady-state and pre-steady-state conditions.

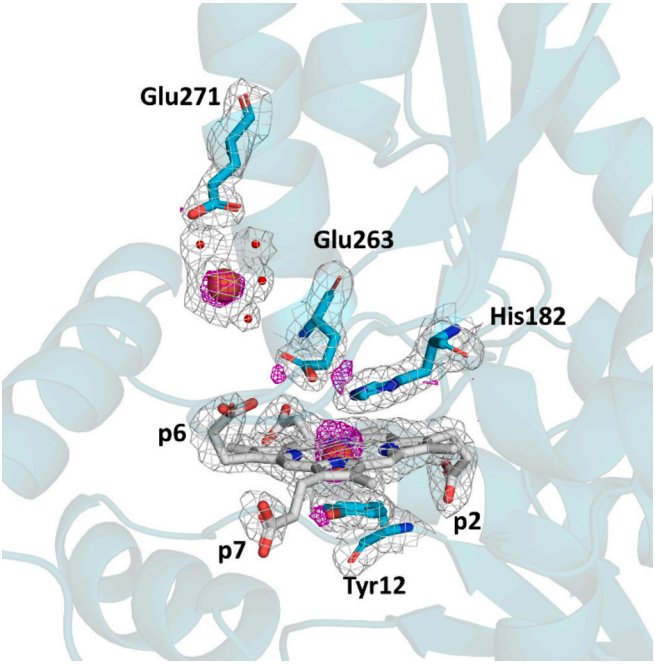

Fig. 2. Anomalous data X-ray crystallography soaking experiment. Structure of WT *Lm*CpfC in complex with coproporphyrin III soaked with Fe^{2+} (PDB ID: 9F0F) with the distal (His182 and Glu263), proximal (Tyr12) residues and potential regulatory site (Glu271). Electron density maps (2fo-fc) are visible as grey meshes (σ = 1.0) and anomalous densities of iron as magenta meshes (σ = 3.0). (For interpretation of the references to colour in this figure legend, the reader is referred to the web version of this article.)

3.1. Spectroscopic study of the imidazole binding

3.1.1. Wild-type protein

The UV–vis electronic absorption spectra of ferric WT *Lm*CpfC – coproheme complex at alkaline pH upon imidazole titration are shown in Fig. 3, left. The binding of imidazole to the native protein results in a shift and a sharpening of the Soret band maximum from 397 to 402 nm with a concomitant redshift of the Q-bands (from 497 and 527 nm to 522 and 548 nm, respectively). Furthermore, the charge transfer band, observed at 618 nm, disappears upon imidazole titration. All these features indicate a change in the heme iron ligation from a Fe-O_{Tyr} pentacoordinated high spin (5cHS) form [7,22] to a hexacoordinated low spin (6cLS) species. The RR spectra in the high wavenumber region (Fig. 3, right), confirm the formation of a 6cLS, characterized by the core size marker bands at 1377 (ν_4), 1508 (ν_3), 1597 (ν_2) and 1642 (ν_{10}) cm^{-1}, at the expense of the 5cHS species [core size marker bands at 1372 (ν_4), 1492 (ν_3), 1584 (ν_2) and 1630 (ν_{10}) cm^{-1}] upon increasing the imidazole concentration. At 140 mM of imidazole, only a 6c bis-Im species is observed. The close similarity of the UV–vis and RR spectra of this 6cLS species with those of the bis-Im complex of the coproheme-myoglobin adduct, as obtained upon addition of imidazole, suggests that the imidazole binds to both the proximal and distal coordination positions of the WT *Lm*CpfC coproheme iron [41].

In the RR spectrum, the intensity ratio ν_4/ν_3 of the 5cHS species increases immediately after the addition of imidazole, suggesting also a change in the fifth ligand of the coproheme iron from the Tyr12 to a strong ligand, like the nitrogen of an imidazole molecule. This possibility is confirmed by the upshift of the Soret band (identified from 398 to 404 nm in the second derivative spectra from 0 to 60–80 mM of imidazole), as heme proteins with a tyrosinate ligand are characterized by a downshifted Soret band maximum with respect to heme proteins with a strong coordinated ligand [42–48].

Upon reduction, we have already reported that the proximal Tyr12 is

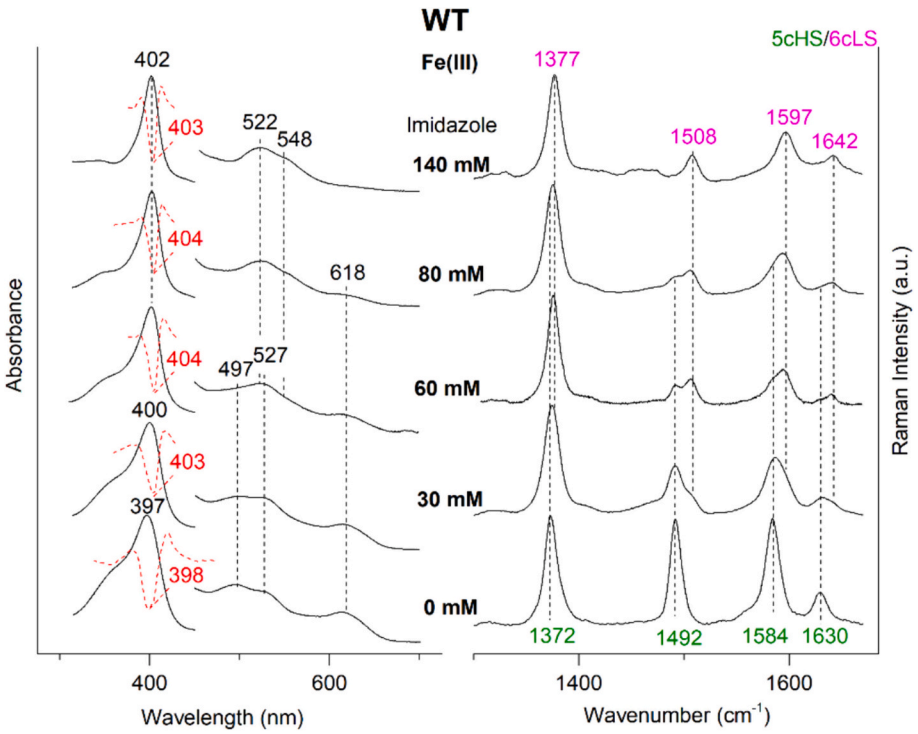

Fig. 3. Spectroscopic study of imidazole binding to WT *Lm*CpfC - ferric coproheme complex. (Left) UV − vis absorption (solid black lines) and second derivative spectra (dotted red lines), and (right) RR spectra in the high wavenumber region of the ferric WT *Lm*CpfC-coproheme complex upon imidazole titration (0, 30, 60, 80, 140 mM), obtained with the 404.8 nm excitation wavelength. The wavenumbers of the RR core size marker bands are indicated in green and purple for the 5cHS and 6cLS species, respectively. (For interpretation of the references to colour in this figure legend, the reader is referred to the web version of this article.)

not completely bound to the iron atom of coproheme, resulting in a mixture of tetracoordinated intermediate spin (4cIS) and 5cHS ferrous forms (Figs. 4 and 5) [22]. The observed broad Soret band is resolved in the second derivative spectrum in multiple peaks (Fig. 4): the minima at 438, 423 and 410 nm are assigned to the 0–0, 0–1 and 0–2 vibrational structures of the 4cIS species, respectively, while the 0–0 and 0–1 electronic transitions of the 5cHS are possibly overlapped in the minima at 423 and 410 nm, respectively [22]. In addition, the band at 388 nm is assigned to the N-band, in analogy to other ferric heme proteins [49]. Upon addition of 140 mM of imidazole, the UV–vis spectra become typical of a 6cLS species (Soret band at 410 nm, Q-bands at 517 and 547 nm) [50], similar to the corresponding ferric form.

The RR spectra of the WT without imidazole, in the high wavenumber region, obtained with both the 404.8 and 441.6 nm excitations, show core size marker bands typical of 5cHS [1358 (ν_4), 1471 (ν_3), 1554 (ν_{11}), 1585 (ν_2) and 1610 (ν_{10}) cm^{-1}] and 4cIS [1371 (ν_4), 1505 (ν_3), 1568 (ν_{11}), 1594 (ν_2) and 1641 (ν_{10}) cm^{-1}] species (Fig. 5) [22]. In agreement with the UV–vis spectra, upon imidazole binding, the formation of a new 6cLS species [1360 (ν_4), 1492 (ν_3), 1549 (ν_{11}), 1600 (ν_2) and 1623 (ν_{10}) cm^{-1}] is observed, and at an imidazole concentration of 140 mM, it remains the only species.

We cannot exclude the presence, during the titration, of a 5cHS species containing as a fifth ligand an imidazole in place of the native Tyr12. As from the core size marker band region it is not possible to distinguish whether the 5c species is due to the Fe-O_{Tyr} (without Im) or to the Fe-N_{Im} (with Im). In addition, the formation of different species during the titration is quantitatively difficult to follow due to the different enhancement of their resonance Raman spectra. The 4cIS species is characterized by an intensified RR spectrum upon 441.6 nm excitation [22] (Fig. 5, right). Similarly, the 5cHS species, with either Fe-O_{Tyr} or Fe-N_{Im} ligation, is expected to show an intensified RR spectrum with excitation on the red side of its Soret band at 423 nm (as for 441.6 nm excitation wavelength) [22,51,52].

However, for a ferrous Fe-N_{Im} 5cHS species, in the low wavenumber region, a strong ν(Fe-N_{Im}) vibration is expected between 200 and 260 cm^{-1} [53]. This band is enhanced upon excitation in resonance with the Soret, via a coupling mechanism involving mixing of the antibonding Fe-

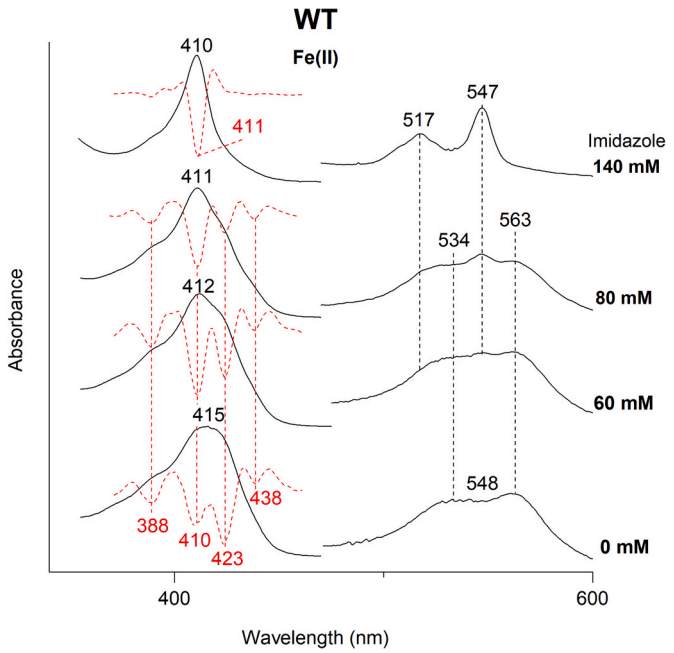

Fig. 4. UV–vis spectra of imidazole binding to WT *Lm*CpfC - ferrous coproheme complex. UV − vis absorption (solid black lines) and second derivative spectra (dotted red lines) of the ferrous WT *Lm*CpfC-coproheme complex upon imidazole titration (0, 60, 80, 140 mM). (For interpretation of the references to colour in this figure legend, the reader is referred to the web version of this article.)

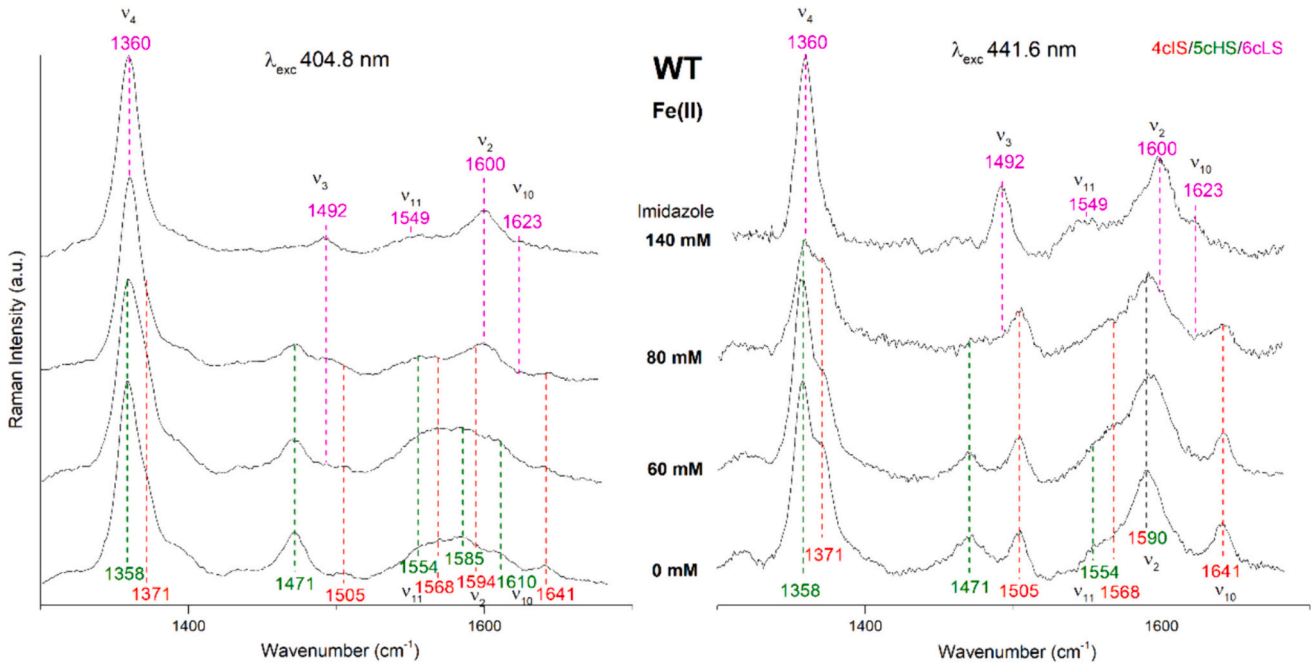

Fig. 5. RR spectra of imidazole binding to WT *Lm*CpfC - ferrous coproheme complex. RR spectra in the high wavenumber region of the ferrous WT *Lm*CpfC-coproheme complex upon imidazole titration (0, 60, 80, 140 mM) obtained with the 404.8 nm (left) and 441.6 nm (right) excitation wavelengths. The wavenumbers of the RR core size marker bands are indicated in green, red, and purple for the 5cHS, 4cIS and 6cLS species, respectively. (For interpretation of the references to colour in this figure legend, the reader is referred to the web version of this article.)

His orbital with the porphyrin π* orbitals [54,55]. Without imidazole, the RR spectra of the WT protein at pH 7.4 and pH 8.5 [22] do not show any ν(Fe-N_{Im}) vibration (Fig. 6), being the bands at 195 cm^{-1} (obtained with the 404.8 nm excitation) and 211 cm^{-1} (obtained with the 441.6 nm excitation) assigned to the ν_{34} and ν_{53} porphyrin vibrational modes, respectively, in analogy to ferrous Mb [56]. Upon the addition of 60 mM of imidazole, an intensity increase is observed at 213 cm^{-1} with the 441.6 nm excitation (i.e., in resonance with the 5c species). This new band is not present in the RR spectrum upon 404.8 nm excitation and is, therefore, assigned to a ν(Fe-N_{Im}) stretching mode. As the 6cLS population increases (at imidazole concentrations equal to or higher than 80 mM), the ν(Fe-N_{Im}) stretching mode is no longer observed and only the ν_{34} and ν_{53} modes are detected at 195 and 211–216 cm^{-1}, respectively. These results indicate the formation of 5cHS with a Fe-N_{Im} ligand at 60 mM of imidazole, which coexists with a very small amount of a 6cLS bis-Im species. In fact, in this region, the ν_8 mode can be taken as a marker band to distinguish the two coexisting species. This mode is observed at 338 cm^{-1} in the 5cHS form and shifts to 348 cm^{-1} in the 6cLS bis-Im complex. At 60 mM of imidazole, in the spectra obtained in resonance with the 404.8 nm excitation wavelength the broadening and

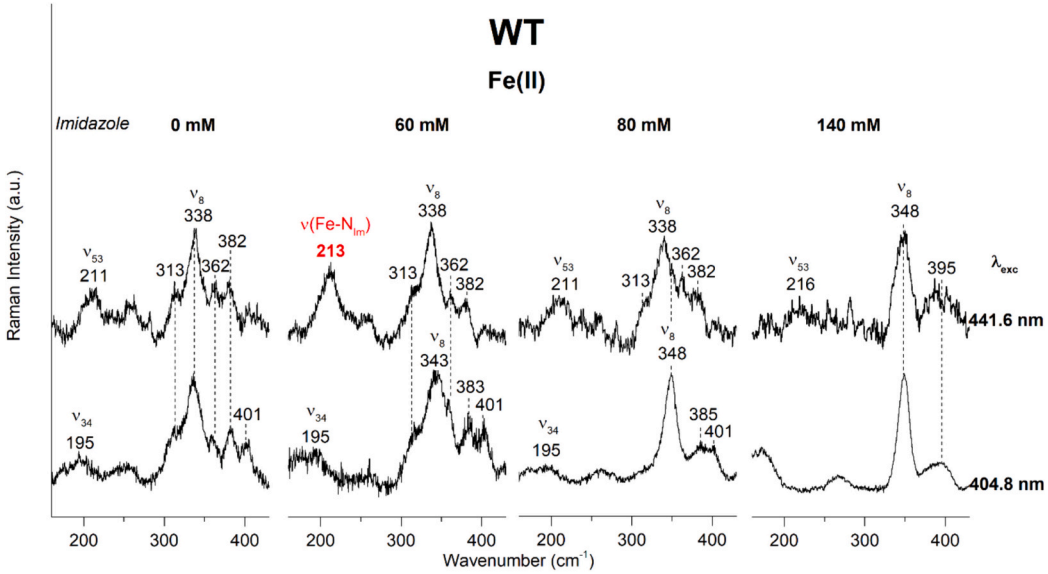

Fig. 6. Low wavenumber region of the RR spectra of imidazole binding to WT *Lm*CpfC - ferrous coproheme complex. RR spectra in the low wavenumber region of the ferrous WT *Lm*CpfC-coproheme complex upon imidazole titration (0, 60, 80 and 140 mM) obtained with the 404.8 nm (bottom) and 441.6 nm (top) excitation wavelengths. The ν(Fe-N_{Im}) wavenumber is indicated in red. The ν_{34} and ν_{53} porphyrin vibrational modes are assigned according to ref. [56]. (For interpretation of the references to colour in this figure legend, the reader is referred to the web version of this article.)

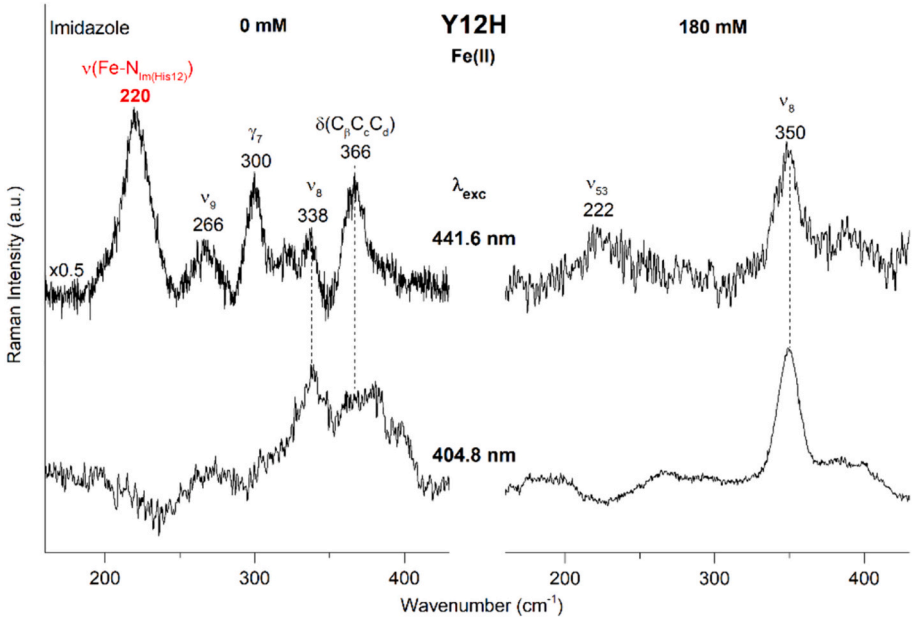

Fig. 7. Low wavenumber region of the RR spectra of imidazole binding to Y12H *Lm*CpfC - ferrous coproheme complex. RR spectra in the low wavenumber region of the ferrous Y12H variant *Lm*CpfC-coproheme complex without imidazole (0 mM) and at the end of the titration (180 mM). The ν(Fe-$N_{Im(His12)}$) wavenumber is indicated in red. The bands at 222, 266 and 300 cm^{-1} are assigned according to refs. [56, 57]. (For interpretation of the references to colour in this figure legend, the reader is referred to the web version of this article.)

upshift of the ν_8 mode to 343 cm^{-1} confirm the presence of both the coordination states. Upon further addition of imidazole (from 80 mM up to the end of the titration), as increasing the hexacoordinated population, the ν_8 mode at 348 cm^{-1} is observed with both the excitation wavelengths.

Based on the results obtained on the WT, we have designed site-directed variants to assess the mechanistic role in ligand binding of the active site residues. We have analysed two distal variants (H182A and E263Q) and one proximal (Y12H) variant.

3.1.2. *Variant on the proximal site (Y12H)*

In the ferric Y12H variant, replacing the proximal native Tyr12 with a His induces an overall redshift of the UV–vis spectra. In the RR spectra, as compared to the WT, the change in the proximal ligand of iron results in an increased ν_4/ν_3 band intensity ratio, typical of a ferric 5cHS species with a proximal His ligand [22] and an upshift of 4–5 cm^{-1} of the ν_3 and ν_{10} bands (Fig. S1). Then, upon the addition of imidazole, the 5cHS population decreases giving rise to a 6cLS bis-Im complex [1376 (ν_4), 1507 (ν_3), 1595 (ν_2) and 1641 (ν_{10}) cm^{-1}], which becomes the only species upon addition of 180 mM of imidazole.

The ferrous Y12H at both neutral [22] and alkaline pH (Fig. S2) shows a predominant 5cHS population [Soret band at 421 nm with a shoulder at 416 nm, resolved into two peaks at 414 and 424 nm in the second derivative spectrum; core size RR bands at 1360 (ν_4), 1473 (ν_3), 1554 (ν_{11}), 1584 (ν_2) and 1610 (ν_{10}) cm^{-1}] with a very small amount of 4cIS [22]. Upon addition of 180 mM imidazole, the resulting UV–vis and RR spectra are similar to the ferrous WT at the end of the titration [Soret band at 410 nm (411 nm in D^2), Q-bands at 517 and 547 nm; RR core size bands at 1360 (ν_4), 1492 (ν_3), 1545 (ν_{11}), 1600 (ν_2) and 1623 (ν_{10}) cm^{-1}], confirming the formation of a bis-Im adduct (Fig. S2).

In the low wavenumber region (Fig. 7), without imidazole the strong band observed at 220 cm^{-1}, intensified upon Soret excitation (i.e., at 441.6 nm excitation), is assigned to the ν(Fe-$N_{Im(His12)}$) [22]. This mode disappears upon imidazole binding due to the formation of the 6cLS bis-Im complex, being the band observed at 222 cm^{-1} assigned to the ν_{53} mode.

3.1.3. *Distal site variants (E263Q, H182A)*

The distal active site variant where the Glu263 was replaced with a Gln (E263Q variant) shows the same spectral features of the native protein, typical of a 5cHS ferric species with a Fe-O_{Tyr} ligation (Fig. S3A) [21]. On the contrary, in the other distal variant where the distal His182 was replaced with an Ala (H182A variant), an additional minor hexacoordinated high spin (aquo 6cHS) population [RR bands at 1484 (ν_3) and 1568 (ν_{10}) cm^{-1}] (Fig. S3B-C) is observed. The presence of a water molecule coordinating the iron atom is confirmed by the X-ray crystallographic structure of the H182A *Lm*CpfC – coproheme complex (PDB ID: 9F0G; Fig. S4). Both ferric variants fully bind the imidazole giving rise to a 6cLS bis-Im complex similar to that observed for the native protein but at different concentrations of imidazole, i.e. 800 mM (E263Q) and 5 mM (H182A).

In the ferrous form, both distal variants are characterized by UV–vis absorption spectra typical of a 5cHS complex, with a broad Soret band at 413–417 nm, a shoulder at 419–421 nm and Q-bands at 540 and 555–560 nm. The RR spectra confirm the presence of a 5cHS species [ν_4 at 1358, ν_3 at 1471, ν_{11} at 1554, ν_2 at 1583 and ν_{10} at 1608–1609 cm^{-1}] (Fig. S5). For the E263Q variant, a minor 4cIS species was also detected with the 441.6 nm excitation wavelength (Fig. 8). Similarly to the ferric form, the imidazole binds both the coordination positions of the ferrous iron, giving rise to a bis-Im complex (6cLS) (Figs. 8 and S5). For the H182A variant, in the low wavenumber region, no ν(Fe-N_{Im}) mode is observed between 0 and 5 mM imidazole (data not shown). On the

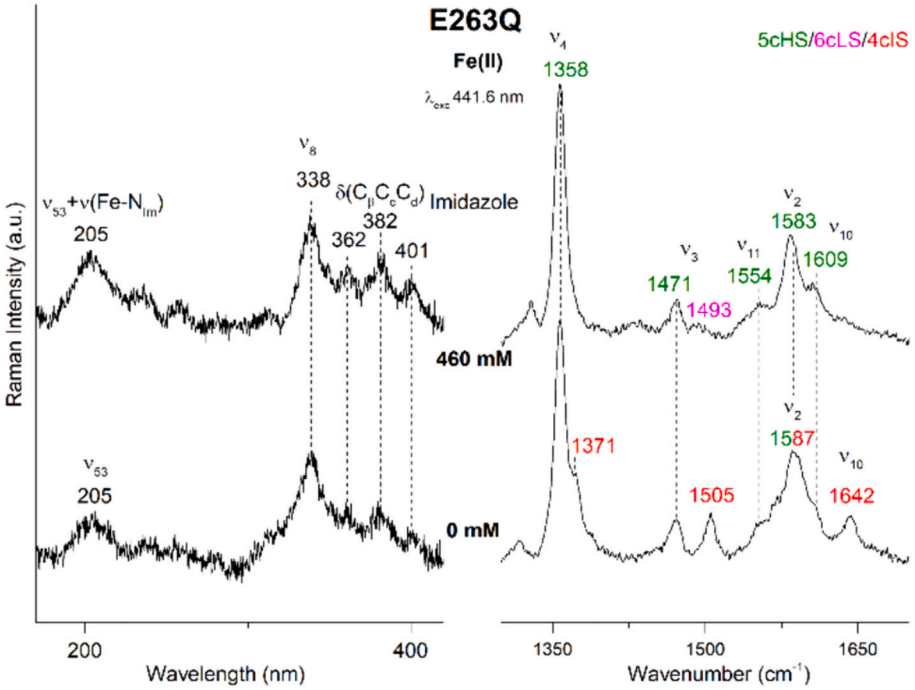

Fig. 8. RR spectra of imidazole binding to E263Q *Lm*CpfC - ferrous coproheme complex. (Left) RR spectra in the low and (Right) high wavenumber regions of the ferrous E263Q variant *Lm*CpfC-coproheme complex upon imidazole titration (0, 460 mM) obtained with the 441.6 nm excitation wavelength. The ν_{53} porphyrin vibrational mode is assigned in analogy to ref. [56]. The ν(Fe-N_{Im}) stretching mode is tentatively assigned overlapped with the ν_{53} vibration. The wavenumbers of the RR core size marker bands are indicated in green, purple, and red the 5cHS, 6cLS and 4cIS species, respectively. (For interpretation of the references to colour in this figure legend, the reader is referred to the web version of this article.)

contrary, for the E263Q variant upon the addition of 460 mM imidazole, the core size marker band region of the 441.6 nm excitation spectrum indicates that the 4cIS species completely disappears, while a 5cHS major population with a small amount of 6cLS (ν_2 at 1493 cm^{-1}) is detected. Concomitantly, in the low wavenumber region, an intensity enhancement of the band at 205 cm^{-1} is observed, which is tentatively assigned to a ν(Fe-N_{Im}) stretching mode overlapped with the ν_{53} vibration observed without imidazole (Fig. 8).

3.2. Kinetic study of the imidazole binding

According to the spectroscopic results, we first tested imidazole binding to the WT *Lm*CpfC - coproheme complex at neutral and alkaline conditions (Fig. 9 and Table 1) under steady-state and pre-steady-state conditions. The steady-state titrations were followed by UV–vis absorption spectroscopy and the change of absorbance at the Soret maximum was plotted against the imidazole concentration, the resulting plots at both pH conditions can be fitted best using the Hill equation with a *n* coefficient larger than 1, resulting in a sigmoidal function. This strongly indicates a cooperative binding mechanism, with two binding sites positively influencing each other. The resulting overall K_D values were determined to be 54.9 ± 1.6 mM at pH 7.4 (Fig. 9A) and 61.5 ± 2.4 mM at pH 8.5 (Fig. 9B). We further investigated this binding reaction under pre-steady-state conditions using UV–vis absorption stopped-flow spectroscopy. Insets of Fig. 9 show representative time traces with clear biphasic behavior. Therefore, each phase was fitted using a single-exponential function, as depicted, and the obtained k_{obs1} and k_{obs2} values were plotted against the imidazole concentration. Both phases proved to be dependent on the imidazole concentration. From the slope of the linear fit of this plot, the bimolecular rates of both binding events (k_{on1} and k_{on2}) can be determined.

Since the findings obtained from the imidazole binding studies to WT *Lm*CpfC strongly suggest the presence of two binding sites, we have extended the study to proximal (Y12H) and distal (E263Q and H182A) site-directed variants to assess their impact on the imidazole binding kinetics (Fig. 10 and Table 1).

Steady-state kinetics (Fig. 10A) of imidazole binding yield a K_D value of 21.6 ± 0.3 mM in the Y12H variant and interestingly also a cooperative behavior, even though the proximal histidine side chain and the imidazole ligand are very similar. On the other hand, the manipulation on the distal side has a drastic effect on the imidazole binding. The replacement of the conserved distal histidine with small alanine in H182A results in a much higher imidazole affinity (K_D = 1.1 ± 0.6 mM) than the WT and in a loss of cooperativity, as the *n* value is close to 1 fitting the data with the Hill equation (Fig. 10B). However, unlike the WT, the resulting fit has the shape of a hyperbolic function that suggest only one binding site (according to the *n* value) or two binding sites with the same, or very close, affinity for the ligand [39,40]. This hypothesis is reinforced by the rather large reported error in the *n* and K_D values determination (Table 1), suggesting a non-ideal data representation in terms of a single process, even if two separate processes cannot be easily disentangled. An opposite effect is observed when the negatively charged conserved distal glutamate is exchanged with a glutamine residue (E263Q variant). The affinity towards imidazole strongly decreases (K_D = 634± 33 mM) and the cooperativity increases compared to the wild-type (Fig. 10C). Examination of the pre-steady-state kinetics of all

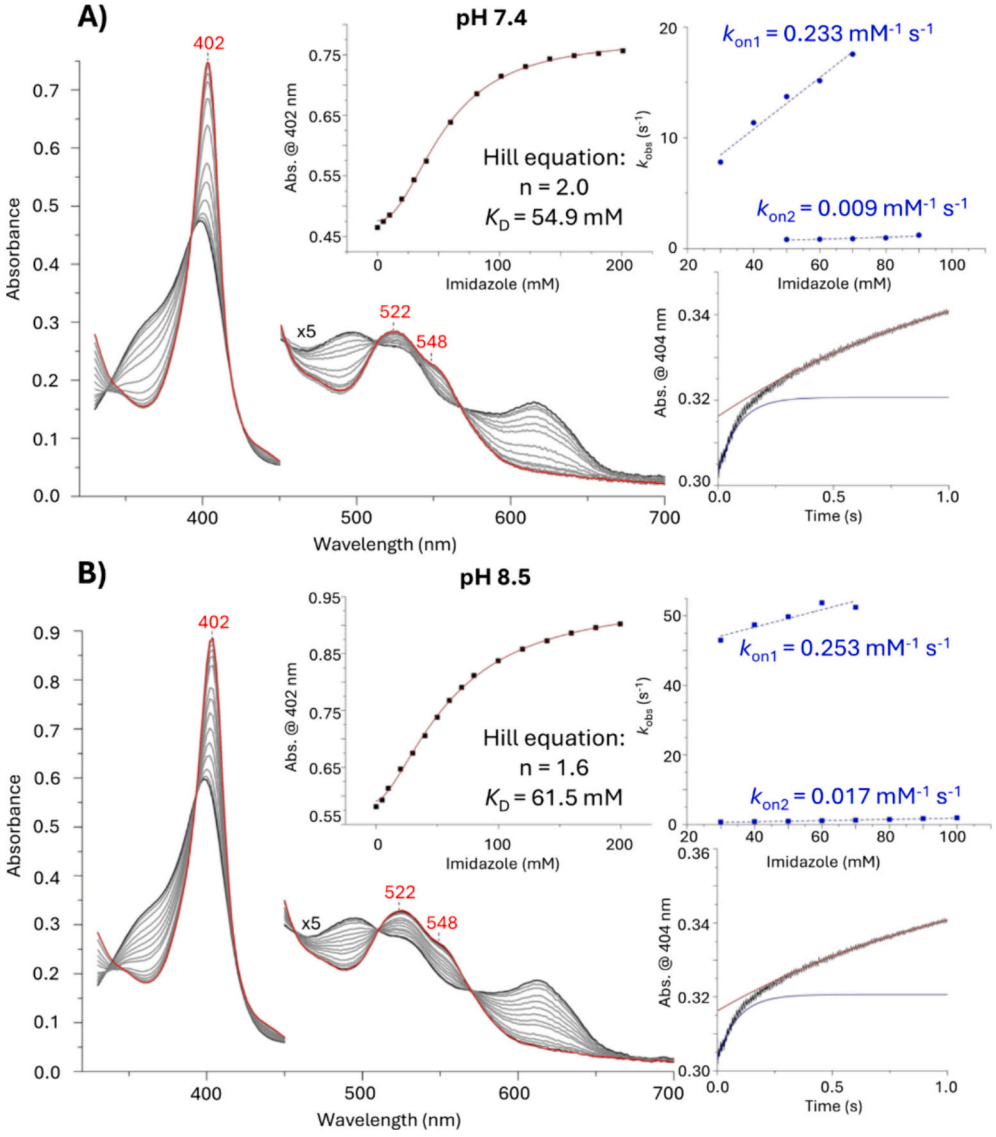

Fig. 9. Imidazole binding and pre-steady-state kinetics of imidazole binding by WT *Lm*CpfC – coproheme complex at different pH. Imidazole titration of 5 μM WT *Lm*CpfC – coproheme complex (black) at neutral (A) and alkaline pH (B) to the complete imidazole binding (red), the intermediate spectra during the titration are reported in grey. The insets show the change in absorbance on the Soret maximum (402 nm) with increasing imidazole concentration together with the Hill equation fitting (red) and the calculated coefficients (n, K_D); the dependence of k_{obs} versus imidazole concentration for the determination of the k_{on1} and k_{on2} (mM^{-1} s^{-1}); the representative time trace at 404 nm of the binding of imidazole with two single exponential fits (red and blue). The calculated errors on the kinetic parameters are reported in Table 1. (For interpretation of the references to colour in this figure legend, the reader is referred to the web version of this article.)

variants emphasizes the presence of one fast binding phase (k_{on1}) and a second slower one (k_{on2}) for the wild-type, the Y12H and the E263Q variant (Fig. 10D). Unfortunately, it was impossible to determine reliable pre-steady-state kinetic parameters for the H182A variant, due to the very fast imidazole binding. Most of its binding reaction and the establishment of the steady-state-equilibrium already occurred within the dead time of the instrumentation (1 ms), at every tested imidazole concentration.

Table 1
Kinetics constants for imidazole binding. Dissociation constant (K_D) and Hill coefficient (n) calculated from the change in absorbance on the Soret maximum with increasing imidazole concentration and association (k_{on1} and k_{on2}) rates calculated from the plots of k_{obs} versus imidazole concentration (Figs 9 and 10) for WT and Y12H, H182A, E263Q variants of *Lm*CpfC – coproheme complex. The calculated errors are also reported.

	n-factor	K_D (mM)	k_{on1} (mM^{-1} s^{-1})	k_{on2} (mM^{-1} s^{-1})
WT neutral pH	2.0 ± 0.1	54.9± 1.6	0.233± 0.020	0.009± 0.002
WT alkaline pH	1.6 ± 0.1	61.5± 2.4	0.253 ± 0.056	0.017 ± 0.001
Y12H alkaline pH	1.8 ± 0.1	21.6± 0.3	0.214 ± 0.005	0.009 ± 0.001
H182A neutral pH	0.7 ± 0.4	1.1 ± 0.6	–	–
E263Q neutral pH	3.1 ± 0.4	634 ± 33	0.394 ± 0.031	0.006 ± 0.001

4. Discussion

A pressing open mechanistic question in the physiological process of iron metalation of porphyrin catalyzed by CpfCs concerns the ferrous iron entry path to the active site. In a first attempt to address this question, we have performed X-ray diffraction experiments of WT *Lm*CpfC - coproporphyrin III crystals soaked with ferrous iron solution to localize the iron-binding site using the anomalous iron signal (Fig. 2). Together with the most prominent signal in the porphyrin center from the formed coproheme, the distal regulatory site (Glu271) is fully occupied with iron. Anomalous electron density blobs are also observed

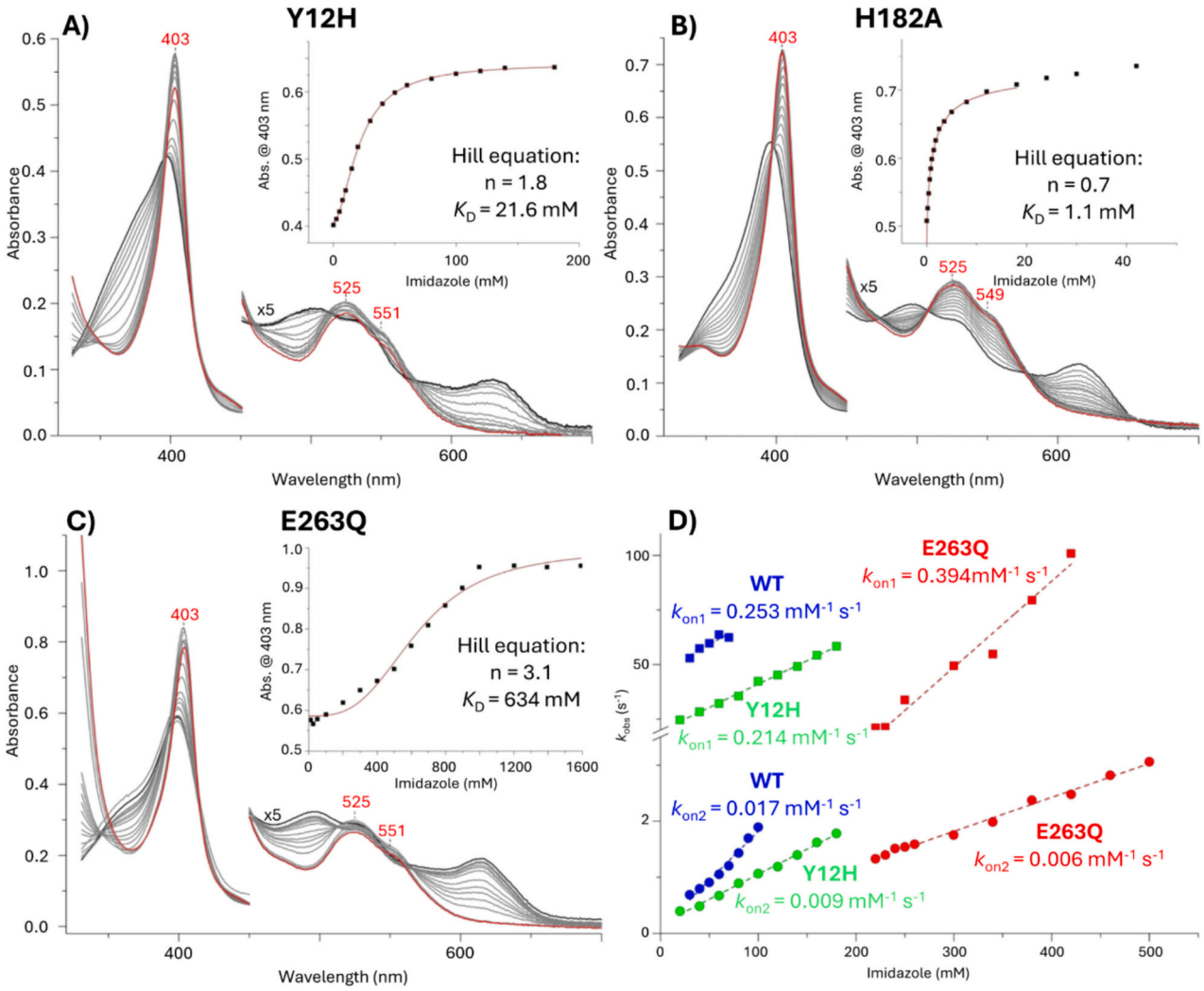

Fig. 10. Imidazole binding by WT and variants of *Lm*CpfC – coproheme complex. Imidazole titration of 5 μM Y12H (A), H182A (B) and E263Q (C) variants of *Lm*CpfC – coproheme complex (black) to the complete imidazole binding (red), the intermediate spectra during the titration are reported in grey. The insets show the change in absorbance on the Soret maximum with increasing imidazole concentration with the Hill equation fitting (red) and the calculated coefficient (n, K_D). (D) Plots of k_{obs} versus imidazole concentration for WT (blue), Y12H (green) and E263Q (red) *Lm*CpfC for the determination of the k_{on}. The kinetic parameters together with calculated errors are reported in Table 1. (For interpretation of the references to colour in this figure legend, the reader is referred to the web version of this article.)

between the distal conserved His182 and Glu263. This is in agreement with previous studies of iron bound to CpfC from *Bacillus subtilis*, although no porphyrin was present in the active site in that study [20]. However, an anomalous X-ray scattering signal, derived from ferrous iron, is further identified on the proximal side of the porphyrin near to Tyr12. This leaves open the question of the direction from which the iron reaches the active site.

In a next step, we have designed a system with a model ligand to probe the possible substrate access channels to the active site, performing a thorough spectroscopic characterization of the significant points of the imidazole titration in combination with experiments on the kinetics of imidazole binding to coproheme-*Lm*CpfC.

The native protein complexed with the coproheme is a 5cHS species, with a coordination between the proximal Tyr12 and the ferric iron atom [7,22], as observed by the similar intensity of the ν_4 and ν_3 vibrational modes in solution (Fig. 3). A small intensity ratio ν_4/ν_3 is typical of proteins with a weak bond between the iron atom and an axial oxygen anionic ligand [42,58–61]. The RR spectra show that, upon the first addition of imidazole, a new 6cLS starts to form at the expense of the 5cHS species. However, the increase of the intensity ratio ν_4/ν_3 of the 5cHS species together with the red-shift of the Soret band observed at the beginning of the titration, suggest also a change in the fifth ligand of the heme iron from the Tyr12 to a strong ligand, like the nitrogen of an imidazole molecule.

Determination of the dissociation constant (K_D) under steady-state conditions showed that the data could be fitted best using a sigmoidal function, modeled by the Hill equation. Consequently, the presence of two binding sites, positively influencing each other were identified. The resulting overall K_D values were slightly pH-dependent in the range of 54.9–61.5 mM (Fig. 9B), and saturation was reached between 150 and 200 mM. Full binding in *Lm*CpfC wild-type upon addition of 140 mM of imidazole is observed in the RR spectrum, which becomes typical of a bis-Im 6cLS species [41]. Therefore, both the spectroscopic and kinetic studies lead to the conclusion that imidazole binds to both the proximal and distal sides.

Imidazole binding was also investigated under pre-steady-state conditions using UV–vis absorption stopped-flow spectroscopy to calculate the k_{on1} and k_{on2} from the observed k_{obs1} and k_{obs2} values plotted against the imidazole concentration. In particular, at alkaline pH two rates were identified, in agreement with the biphasic time traces (Figs. 9, 10 and Table 1), which differ by over 10-fold (k_{on1} = 0.253 ± 0.056 mM^{-1} s^{-1}, k_{on2} = 0.017± 0.001 mM^{-1} s^{-1}). The faster binding event is likely to take place on the distal site, which is free from any interactions, while the slower binding happens on the proximal site

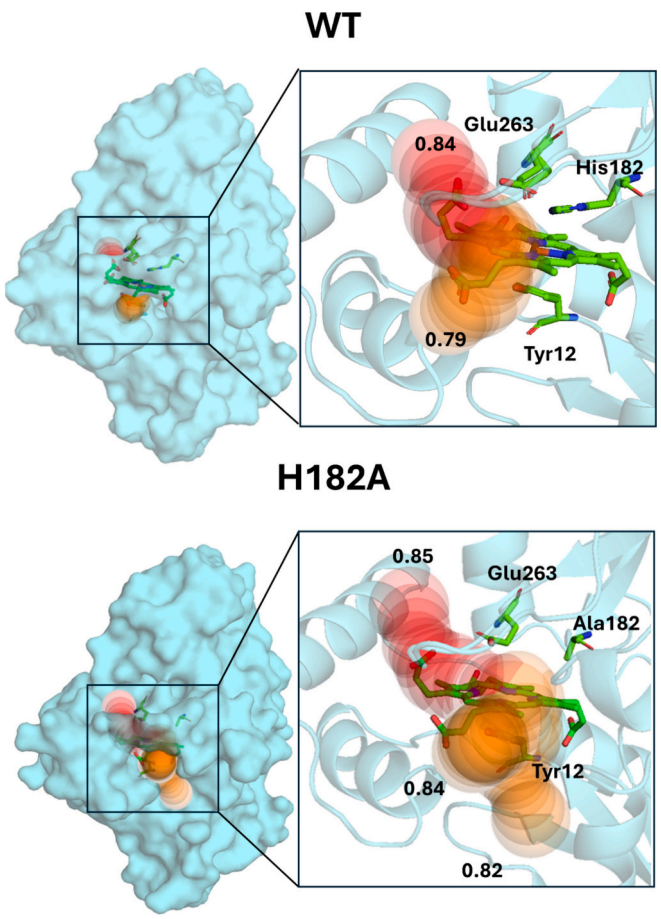

Fig. 11. Substrate access channels. Representation of the substrate access channels as colored spheres for WT (PDB ID: 6SV3) and H182A (PDB ID: 9F0G) variant of *Lm*CpfC – coproheme complex and calculated priority parameters (black). Two main pathways, one distal (red) and one proximal (orange), are observed for the WT. For the H182A also a third one (orange) was observed. Calculations were performed with CAVER 3.0 PyMOL plugin [64]. Settings: Minimum probe radius = 0.9; Shell depth = 8; Clustering threshold = 4; Input model = only all respective amino acids; Starting point = central porphyrin metal; Starting point optimization – maximum distance = 3; desired radius = 5. The distal (Glu263, His182 or Ala182) and proximal (Tyr12) residues of the active site are also represented. Only the channels with a throughput higher than 0.75 are shown. While all the channels are show in Fig. S6 and, in Table S3, the tunnel characteristics are reported. (For interpretation of the references to colour in this figure legend, the reader is referred to the web version of this article.)

where the porphyrin iron is initially bound to Tyr12. The kinetic studies thus lead to the conclusion that the imidazole first binds to the distal side, disrupting the proximal Tyr12-iron ligation and giving rise to a new 5cHS Fe-N_{Im} species. Then the second imidazole molecule binds to the proximal site, as the 6cLS bis-Im population increases. In agreement with the suggestion that an exogenous ligand binds first the distal side with the concomitant loss of the proximal Fe-coordination are the results obtained previously on CO binding, which gives rise to a conformer characterized by weak or no trans ligand [62]. Moreover, in the resting state and during turnover, a weak or non-existing proximal coordination of the coproheme iron is fundamental for the transient binding of Fe^{2+} as a substrate and the release of the final coproheme product in bacterial ferrochelatases [22].

By using UV–vis and RR spectroscopies it is possible to follow the binding of exogenous imidazole to coproheme-*Lm*CpfC also in the ferrous form; however, the situation is more complex than in the ferric state. The reduced form of the wild-type *Lm*CpfC – coproheme complex is a mixture of 4cIS and 5cHS species as, upon reduction, the Fe-Tyr12 interaction is partially broken [22]. As for the ferric form, imidazole binds readily in the ferrous state. In the high wavenumber region, the core size marker bands (Fig. 5), show the formation of a new 6cLS bis-Im population at the expense of the initial 4c and 5c species upon imidazole addition. It can be noted that the binding is completed at an imidazole concentration of 140 mM for both the ferric and ferrous forms, suggesting that the affinity to the exogenous imidazole is the same in the oxidized and reduced states of the coproheme complex. From the RR high wavenumber region it is difficult to evaluate whether, at an intermediate concentration of imidazole (60–80 mM), the binding of the ligand results in the breaking of the iron-Tyr12 interaction (a new 5c Fe-N_{im} species) or not (i.e., the initial Fe-O_{Tyr12} species). However, ferrous 5c hemeproteins with a Fe-N_{Im} present a strong band between 200 and 260 cm^{-1} [53], due to the ν(Fe-N_{Im}) stretching vibration. Therefore, in the low wavenumber region of the RR spectra an imidazole bound to the iron (Fig. 6) can be identified. Upon the addition of 60 mM of imidazole a new band at 213 cm^{-1} is observed upon excitation in resonance with the Soret band of the 5c species (at 441.6 nm excitation wavelength), not present either upon excitation outside the Soret band (at 404.8 nm excitation wavelength) or in the WT – coproheme complex without the addition of imidazole [22]. This band is, therefore, assigned to the ν(Fe-N_{Im}) of the adduct with the exogenous imidazole. The comparison of the wavenumber of the ν(Fe-N_{Im}) stretching mode of the WT-imidazole ligated protein and the Y12H variant [22], at 213 and 220 cm^{-1}, respectively, suggests a stronger Fe-N_{Im} bond for the Y12H than in the WT. This may be a consequence of a different orientation of the imidazole ring in the active site of the protein [55]. Upon further addition of imidazole (80 mM), a 6cLS population increases and the ν(Fe-N_{Im}) disappears. This is consistent with the imidazole binding studies in the ferric form, where the K_D is around 60 mM (Fig. 9B).

Selected active site variants, one proximal (Y12H) and two distal targeting the conserved His182 and Glu263 residues (H182A and E263Q), were also characterized to assess their impact on imidazole binding kinetics and their mechanistic role in ligand binding.

For the Y12H variant (Fig. 10A) interestingly the cooperative behavior was observed even if the proximal iron coordination site is already occupied by a His12 side chain. The presence of two binding sites was also confirmed by pre-steady-state kinetics. Both binding kinetic are slower compared to that observed for the native protein (k_{on1} = 0.214 ± 0.005 mM^{-1} s^{-1}, k_{on2} = 0.009 ± 0.001 mM^{-1} s^{-1}). The 6cLS population progressively increases at the expense of the 5c population and, at 180 mM, the binding of imidazole is completed, in agreement with the kinetic studies. In the Y12H variant, the initial 5c species is due to the Fe-$N_{Im(His12)}$ interaction, which is spectroscopically identical to the Fe-N_{Im} species formed during imidazole binding and, therefore, it is impossible to obtain more information on the ferric form.

In the ferrous form, as discussed before [22], the Y12H variant is mainly a 5cHS species with a strong ν(Fe-$N_{Im(His12)}$) vibrational mode at 220 cm^{-1} (Fig. 7). Only a minor 4cIS species is detected with the 441.6 nm excitation wavelength, due to a partial break of the Fe-His12 ligation [22]. The imidazole-fully bound form is almost identical to that of the native protein, being characteristic of a 6cLS bis-Im species. As for the WT, imidazole saturation is independent from the oxidation state of the iron atom. Upon titration with imidazole, we were unable to identify any other ν(Fe-N_{Im}) rather than the ν(Fe-$N_{Im(His12)}$) observed before the addition of imidazole. In the case that the His12 would be replaced by an exogenous imidazole, a change in the wavenumber of the ν(Fe-N_{Im}) mode should be expected, in agreement with the WT results. However, we cannot rule out that the strong intensities of the ν(Fe-$N_{Im(His12)}$) may hide any other ν(Fe-N_{Im}) band formed during imidazole titration.

The change of the conserved distal residues has a drastic effect on the imidazole binding. The replacement of the His182 with the small alanine allows a water molecule to enter into the distal side to bind the iron, as shown by the X-ray crystal structure (Fig. S4) and the RR spectroscopic studies (Fig. S3A). This highly accessible distal cavity

reflects also on the imidazole binding kinetics, which is significantly faster than in the wild-type. The variant has a much-increased imidazole affinity (K_D = 1.1 ± 0.6 mM). The Soret absorbance as a function of imidazole concentration can be best fitted using a hyperbolic function suggesting the loss of cooperativity or the presence of two binding sites, with the same affinity for the ligand (Fig. 10B). The spectroscopic characterization suggests that in both the ferric and ferrous forms, the imidazole binds both the coordination positions giving rise to a 6cLS bis-Im complex (at approximately 5 mM imidazole) (Fig. S5), similarly to the native protein. In the low wavenumber region of the ferrous form, no ν(Fe-N_{Im}) mode is observed suggesting that the binding to both the coordination positions occurs on a timescale faster than the time resolution of our experiments.

An opposite effect is observed when the negatively charged conserved distal glutamate is exchanged with a glutamine residue. The affinity towards imidazole strongly decreases (K_D = 634 ± 33 mM) and the cooperativity increases compared to the native protein (Fig. 10C). Before the addition of imidazole, the ferrous protein is mainly a 5cHS with a minor 4cIS. Upon imidazole binding, a new 6cLS is detected which becomes the only species present at the end of the titrations. In this case, to reach the endpoint of the titration a high imidazole concentration is needed (almost 800 mM), in agreement with the significantly decreased affinity. Upon reduction, as for all the other proteins investigated in this paper, imidazole binding is not highly influenced by the iron oxidation states. Its saturation (with the formation of a 6cLS bis-Im) is always observed at 800 mM. Interestingly, around the K_D value (460 mM) the RR spectra suggest that the 4c disappears, only a 5cHS major population with a minor 6cLS are detected. The band at about 205 cm^{-1} is tentatively assigned, on the basis of its relative intensity as compared to the spectrum without imidazole, to a ν(Fe-N_{Im}) stretching mode overlapped with the ν_{53} vibrational mode. Interestingly, for the E263Q variant it was also reported that the lack of the Glu263 negatively charged amino acid side chain in the active site decreases the capability to oxidize the Fe^{2+} ion during metalation of the porphyrin, and shows an higher reduction potential of the Fe(III)/Fe(II) redox couple of the coproheme complex [21].

The spectroscopic and kinetic characterization confirm the presence of two binding sites for the imidazole in all the investigated proteins. This can be visualized by CAVER calculations for the WT presented in Figs. 11 and S6 [63]. Table S3 lists all the characteristic of the channels calculated by CAVER. The two access paths with the highest priority (throughput: 0.84 and 0.79) clearly indicate that both the proximal and the distal heme sides are accessible. Usually, a channel is considered meaningful, if the throughput is above 0.75 [63]. As we have solved the X-ray crystal structure for the H182A variant of *Lm*CpfC (Fig. S4 and Table S2), CAVER calculations were performed also for this system. They reveal the existence of both a WT-like distal channel and a proximal one, larger than that observed in the WT, which needs to be fitted by two channels (Fig. 11). In fact, in the WT a second proximal channel was not detected even considering the channels with a low throughput (Table S3). The exact reason for the expanded proximal channel in the variant, in which the distal cavity is altered, is not obvious but is the consequence of changes in the second coordination sphere resulting in a slight rearrangement of the alpha-helix close to Tyr12 (Fig. 11). Considering the positions of anomalous scattering densities in the iron soaking experiments, it becomes evident that one observed electron density blob accounts for the distal channel (between His182 and Glu283, Fig. 2) and the other for the proximal channel (next to 12, Fig. 2). The larger proximal channel explains the more accessible active site in this variant and the loss of cooperativity, suggested by the kinetic investigations within this work, by enhancing binding from the proximal side. Moreover, the pre-steady-state kinetics suggest the presence of one fast binding phase (k_{on1}) and a second slower one (k_{on2}) for the wild-type, the Y12H and the E263Q variants (Fig. 10D and Table 1). Based on these data we suggest that the faster binding involves the distal coordination position of the porphyrin iron, which is free from ligand, while the slower binding happens on the proximal site, where the iron atom is ligated to Tyr12. Accordingly, for the E263Q where the mutation concerns the distal side, the first binding is even faster, as compared to the WT, while the proximal binding (i.e., without mutation) is identical to the WT (Table 1). The imidazole binding to the distal side disrupts the proximal Tyr12 iron ligation giving rise to a new 5cHS Fe-N_{im} species. Then, a second imidazole molecule could bind to this iron proximal site. This hypothesis is supported also by the observed positive cooperativity.

5. Conclusion

We have provided evidence by spectroscopic, kinetic, and structural methods that two substrate channels in coproporphyrin ferrochelatases are possible. In details, the use of a model ligand as imidazole for the enzyme from the firmicute representative *Listeria monocytogenes* clearly demonstrates that imidazole binds to both the distal side and the proximal side of the iron porphyrin active site. Furthermore, X-ray crystallographic studies on the in vitro metalation of the porphyrin obtained for this enzyme show anomalous X-ray scattering signals, corresponding to ferrous iron on the distal (His182 and Glu263) and proximal (Tyr12) side, as well as in the porphyrin. Furthermore, the proposed regulatory site (Glu271) is occupied as well.

In this work, we contribute another piece of information at the molecular level to identify the full mechanism of enzymes involved in the coproporphyrin heme biosynthesis pathway of monoderm bacteria. However, the present and previous results are not yet able to explain the details of iron delivery to CpfC's active site, as, this process most probably depends also on protein-protein interactions [6]. The nature of these protein-protein interactions might determine the path of ferrous iron insertion, depending on the interaction site.

CRediT authorship contribution statement

Andrea Dali: Writing – review & editing, Writing – original draft, Methodology, Investigation, Formal analysis, Data curation. **Thomas Gabler:** Writing – review & editing, Methodology, Investigation, Formal analysis. **Federico Sebastiani:** Writing – review & editing, Writing – original draft, Supervision, Methodology, Investigation, Formal analysis, Data curation, Conceptualization. **Paul G. Furtmüller:** Writing – review & editing, Formal analysis, Data curation. **Maurizio Becucci:** Writing – review & editing, Writing – original draft, Data curation, Methodology, Supervision. **Stefan Hofbauer:** Writing – original draft, Writing – review & editing, Supervision, Funding acquisition. **Giulietta Smulevich:** Writing – review & editing, Writing – original draft, Supervision, Project administration, Funding acquisition, Data curation, Conceptualization.

Declaration of competing interest

The authors declare that they have no known competing financial interests or personal relationships that could have appeared to influence the work reported in this paper.

Data availability

Data will be made available on request.

Acknowledgements

This research was funded by the Austrian Science Fund, FWF, projects P34934, W1224, P33544, P36967 (S.H.) and Fondazione Cassa di Risparmio di Firenze, grant 2020.1397 (G.S.). The support of MUR-Italy ("Progetto Dipartimenti di Eccellenza 2023–2027", CUP B97G22000740001 - DICUS 2.0, allocated to the Department of Chemistry "Ugo Schiff") is acknowledged (F.S., M.B., G.S.). A.D. is the recipient of a Ph.D. fellowship funded by MUR-Italy "Progetto Dipartimenti

di Eccellenza 2018–2022", CUP B96C1700020008, and allocated to the Department of Chemistry "Ugo Schiff". This project was supported by EQ-BOKU VIBT GmbH and the Protein Crystallography Unit of the BOKU Core Facility Biomolecular & Cellular Analysis. We would like to thank the staff of the ESRF and EMBL Grenoble for assistance and support in using beamlines ID-23-1 and ID-23-2 (doi: 10.15151/ESRF-ES-1022127512 and 10.15151/ESRF-ES-1018322323) under proposal number MX2455.

Appendix A. Supplementary data

Supplementary data to this article can be found online at https://doi.org/10.1016/j.jinorgbio.2024.112681.

References

[1] D.A. Bryant, C.N. Hunter, M.J. Warren, J. Biol. Chem. 295 (2020) 6888–6925.
[2] J.E. Choby, E.P. Skaar, J. Mol. Biol. 428 (2016) 3408–3428.
[3] H.A. Dailey, S. Gerdes, T.A. Dailey, J.S. Burch, J.D. Phillips, Proc. Natl. Acad. Sci. USA 112 (2015) 2210–2215.
[4] G. Layer, Biochim. Biophys. Acta, Mol. Cell Res. 1868 (2021) 118861.
[5] H.A. Dailey, T.A. Dailey, S. Gerdes, D. Jahn, M. Jahn, M.R. O'Brian, M.J. Warren, Microbiol. Mol. Biol. Rev. 81 (2017).
[6] N. Falb, G. Patil, P.G. Furtmüller, T. Gabler, S. Hofbauer, Comput. Struct. Biotechnol. J. 21 (2023) 3933–3945.
[7] T. Gabler, F. Sebastiani, J. Helm, A. Dali, C. Obinger, P.G. Furtmüller, G. Smulevich, S. Hofbauer, FEBS J. 289 (2022) 1680–1699.
[8] M. Zamocky, S. Hofbauer, T. Gabler, P.G. Furtmüller, Biology (Basel) 12 (2023).
[9] H.A. Dailey, T.A. Dailey, C.K. Wu, A.E. Medlock, K.F. Wang, J.P. Rose, B.C. Wang, Cell. Mol. Life Sci. 57 (2000) 1909–1926.
[10] G.C. Ferreira, R. Franco, S.G. Lloyd, I. Moura, J.J. Moura, B.H. Huynh, J. Bioenerg. Biomembr. 27 (1995) 221–229.
[11] A.I. Celis, G.H. Gauss, B.R. Streit, K. Shisler, G.C. Moraski, K.R. Rodgers, G. S. Lukat-Rodgers, J.W. Peters, J.L. DuBois, J. Am. Chem. Soc. 139 (2017) 1900–1911.
[12] L. Milazzo, T. Gabler, D. Pühringer, Z. Jandova, D. Maresch, H. Michlits, V. Pfanzagl, K. Djinović-Carugo, C. Oostenbrink, P.G. Furtmüller, C. Obinger, G. Smulevich, S. Hofbauer, ACS Catal. 9 (2019) 6766–6782.
[13] H. Michlits, B. Lier, V. Pfanzagl, K. Djinović-Carugo, P.G. Furtmüller, C. Oostenbrink, C. Obinger, S. Hofbauer, ACS Catal. 10 (2020) 5405–5413.
[14] F. Sebastiani, H. Michlits, B. Lier, M. Becucci, P.G. Furtmüller, C. Oostenbrink, C. Obinger, S. Hofbauer, G. Smulevich, Biophys. J. 120 (2021) 3600–3614.
[15] V. Pfanzagl, L. Holcik, D. Maresch, G. Gorgone, H. Michlits, P.G. Furtmüller, S. Hofbauer, Arch. Biochem. Biophys. 640 (2018) 27–36.
[16] H.A. Dailey, A.E. Medlock, Biol. Chem. 403 (2022) 985–1003.
[17] S. Hofbauer, J. Helm, C. Obinger, K. Djinović-Carugo, P.G. Furtmüller, FEBS J. 287 (2020) 2779–2796.
[18] A. Dali, T. Gabler, F. Sebastiani, A. Destinger, P.G. Furtmüller, V. Pfanzagl, M. Becucci, G. Smulevich, S. Hofbauer, Protein Sci. 32 (2023) e4534.
[19] D. Lecerof, M.N. Fodje, R. Alvarez Leon, U. Olsson, A. Hansson, E. Sigfridsson, U. Ryde, M. Hansson, S. Al-Karadaghi, J. Biol. Inorg. Chem. 8 (2003) 452–458.
[20] M.D. Hansson, T. Karlberg, M.A. Rahardja, S. Al-Karadaghi, M. Hansson, Biochemistry 46 (2007) 87–94.
[21] T. Gabler, A. Dali, M. Bellei, F. Sebastiani, M. Becucci, G. Battistuzzi, P. G. Furtmüller, G. Smulevich, S. Hofbauer, FEBS J 291 (2024) 2260–2272.
[22] A. Dali, F. Sebastiani, T. Gabler, G. Frattini, D.M. Moreno, D.A. Estrin, M. Becucci, S. Hofbauer, G. Smulevich, Spectrochim. Acta A Mol. Biomol. Spectrosc. 313 (2024) 124120.
[23] M. Hoggins, H.A. Dailey, C.N. Hunter, J.D. Reid, Biochemistry 46 (2007) 8121–8127.
[24] V.M. Sellers, C.K. Wu, T.A. Dailey, H.A. Dailey, Biochemistry 40 (2001) 9821–9827.
[25] A.E. Medlock, T.A. Dailey, T.A. Ross, H.A. Dailey, W.N. Lanzilotta, J. Mol. Biol. 373 (2007) 1006–1016.
[26] A.E. Medlock, W. Najahi-Missaoui, M.T. Shiferaw, A.N. Albetel, W.N. Lanzilotta, H. A. Dailey, Biochem. J. 478 (2021) 3239–3252.
[27] T. Gabler, A. Dali, F. Sebastiani, P.G. Furtmüller, M. Becucci, S. Hofbauer, G. Smulevich, Protein Sci 32 (2023) e4788.
[28] G.A. Hunter, G.C. Ferreira, Coord. Chem. Rev. 460 (2022) 214464.
[29] M.O. Senge, S.A. MacGowan, J.M. O'Brien, Chem. Commun. (Camb.) 51 (2015) 17031–17063.
[30] T. Karlberg, M.D. Hansson, R.K. Yengo, R. Johansson, H.O. Thorvaldsen, G. C. Ferreira, M. Hansson, S. Al-Karadaghi, J. Mol. Biol. 378 (2008) 1074–1083.
[31] G.C. Ferreira, R. Franco, A. Mangravita, G.N. George, Biochemistry 41 (2002) 4809–4818.
[32] T. Karlberg, D. Lecerof, M. Gora, G. Silvegren, R. Labbe-Bois, M. Hansson, S. Al-Karadaghi, Biochemistry 41 (2002) 13499–13506.
[33] J. Wu, S. Wen, Y. Zhou, H. Chao, Y. Shen, J. Chem. Inf. Model. 56 (2016) 2421–2433.
[34] Y. Wang, Y. Shen, J. Mol. Model. 19 (2013) 963–971.
[35] A.J. McCoy, R.W. Grosse-Kunstleve, P.D. Adams, M.D. Winn, L.C. Storoni, R. J. Read, J. Appl. Crystallogr. 40 (2007) 658–674.
[36] V.B. Chen, W.B. Arendall, J.J. Headd, D.A. Keedy, R.M. Immormino, G.J. Kapral, L. W. Murray, J.S. Richardson, D.C. Richardson, Acta Crystallogr. D Biol. Crystallogr. 66 (2010) 12–21.
[37] C. Hobbs, J.D. Reid, M. Shepherd, Biochem. J. 474 (2017) 3513–3522.
[38] D. Lecerof, M. Fodje, A. Hansson, M. Hansson, S. Al-Karadaghi, J. Mol. Biol. 297 (2000) 221–232.
[39] J.N. Weiss, FASEB J. 11 (1997) 835–841.
[40] S. Goutelle, M. Maurin, F. Rougier, X. Barbaut, L. Bourguignon, M. Ducher, P. Maire, Fundam. Clin. Pharmacol. 22 (2008) 633–648.
[41] L. Milazzo, S. Hofbauer, B.D. Howes, T. Gabler, P.G. Furtmüller, C. Obinger, G. Smulevich, Biochemistry 57 (2018) 2044–2057.
[42] F.P. Nicoletti, B.D. Howes, M. Fittipaldi, G. Fanali, M. Fasano, P. Ascenzi, G. Smulevich, J. Am. Chem. Soc. 130 (2008) 11677–11688.
[43] D.J. Yan, H. Yuan, W. Li, Y. Xiang, B. He, C.M. Nie, G.B. Wen, Y.W. Lin, X. Tan, Dalton Trans. 44 (2015) 18815–18822.
[44] T. Komatsu, N. Ohmichi, A. Nakagawa, P.A. Zunszain, S. Curry, E. Tsuchida, J. Am. Chem. Soc. 127 (2005) 15933–15942.
[45] S. Adachi, S. Nagano, Y. Watanabe, K. Ishimori, I. Morishima, Biochem. Biophys. Res. Commun. 180 (1991) 138–144.
[46] S. Adachi, S. Nagano, K. Ishimori, Y. Watanabe, I. Morishima, T. Egawa, T. Kitagawa, R. Makino, Biochemistry 32 (1993) 241–252.
[47] D.P. Hildebrand, D.L. Burk, R. Maurus, J.C. Ferrer, G.D. Brayer, A.G. Mauk, Biochemistry 34 (1995) 1997–2005.
[48] A.E. Pond, M.P. Roach, M. Sono, A.H. Rux, S. Franzen, R. Hu, M.R. Thomas, A. Wilks, Y. Dou, M. Ikeda-Saito, P.R. Ortiz de Montellano, W.H. Woodruff, S. G. Boxer, J.H. Dawson, Biochemistry 38 (1999) 7601–7608.
[49] M.W.Makinen, A.K. Churg, in: A.B.P. Laver and H.B. Gray (Eds.), Iron Porphyrins, Part 1, Addison-Wesley Publishing Company; Reading, MA: 1983. pp. 141–236.
[50] E. Droghetti, S. Oellerich, P. Hildebrandt, G. Smulevich, Biophys. J. 91 (2006) 3022–3031.
[51] S. Hofbauer, G. Mlynek, L. Milazzo, D. Pühringer, D. Maresch, I. Schaffner, P. G. Furtmüller, G. Smulevich, K. Djinović-Carugo, C. Obinger, FEBS J. 283 (2016) 4386–4401.
[52] F. Sebastiani, R. Risorti, C. Niccoli, H. Michlits, M. Becucci, S. Hofbauer, G. Smulevich, J. Inorg. Biochem. 229 (2022) 111718.
[53] G. Smulevich, B.D. Howes, E. Droghetti, in: E. Raven, B. Dunford (Eds.), Heme Peroxidases, RSC Metallobiology Series, The Royal Society of Chemistry, 2016, pp. 61–98.
[54] T.G. Spiro, X.-Y. Li, Resonance Raman Spectroscopy of Metalloporphyrins, in: T. G. Spiro (Ed.), Biological Applications of Raman Spectroscopy, John Wiley, New York, 1988, pp. 1–38.
[55] O. Bangcharoenpaurpong, K.T. Schomacker, P.M. Champion, J. Am. Chem. Soc. 106 (1984) 5688–5698.
[56] S.Z. Hu, K.M. Smith, T.G. Spiro, J. Am. Chem. Soc. 118 (1996) 12638–12646.
[57] G. Smulevich, S.Z. Hu, K.R. Rodgers, D.B. Goodin, K.M. Smith, T.G. Spiro, Biospectroscopy 2 (1996) 365–376.
[58] Y. Liu, P. Moenne-Loccoz, D.P. Hildebrand, A. Wilks, T.M. Loehr, A.G. Mauk, P. R. Ortiz de Montellano, Biochemistry 38 (1999) 3733–3743.
[59] S. Eakanunkul, G.S. Lukat-Rodgers, S. Sumithran, A. Ghosh, K.R. Rodgers, J. H. Dawson, A. Wilks, Biochemistry 44 (2005) 13179–13191.
[60] G.S. Lukat-Rodgers, K.R. Rodgers, C. Caillet-Saguy, N. Izadi-Pruneyre, A. Lecroisey, Biochemistry 47 (2008) 2087–2098.
[61] S. Hu, J.R. Kincaid, FEBS Lett. 314 (1992) 293–296.
[62] F. Sebastiani, A. Dali, D.J. Alonso de Armino, L. Campagni, G. Patil, M. Becucci, S. Hofbauer, D.A. Estrin, G. Smulevich, J. Inorg. Biochem. 245 (2023) 112243.
[63] A. Pavelka, E. Sebestova, B. Kozlikova, J. Brezovsky, J. Sochor, J. Damborsky, IEEE/ACM Trans. Comput. Biol. Bioinform. 13 (2016) 505–517.
[64] E. Chovancova, A. Pavelka, P. Benes, O. Strnad, J. Brezovsky, B. Kozlikova, A. Gora, V. Sustr, M. Klvana, P. Medek, L. Biedermannova, J. Sochor, J. Damborsky, PLoS Comput. Biol. 8 (2012) e1002708.